Large-scale Physical Modelling Study on the Interaction between Rockfall and Flexible Barrier

by

Dao-Yuan TAN[1]
Department of Civil and Environmental Engineering
The Hong Kong Polytechnic University, Hung Hom, Kowloon, Hong Kong, China
Email: rztdy2009@gmail.com

Jian-Hua YIN[1] (Chair Professor and Corresponding Author)
Department of Civil and Environmental Engineering
The Hong Kong Polytechnic University, Hung Hom, Kowloon, Hong Kong, China
Tel: (852) 2766-6065, Fax: (852) 2334-6389, Email: cejhyin@polyu.edu.hk

Jie-Qiong QIN[1]
Department of Civil and Environmental Engineering
The Hong Kong Polytechnic University, Hung Hom, Kowloon, Hong Kong, China
Email: jieqiong.qin@connect.polyu.hk

Zhuo-Hui ZHU[1]
Department of Civil and Environmental Engineering
The Hong Kong Polytechnic University, Hung Hom, Kowloon, Hong Kong, China
Email: zhuo-hui.zhu@connect.polyu.hk

and

Wei-Qiang FENG[1]
Department of Civil and Environmental Engineering,
The Hong Kong Polytechnic University, Hung Hom, Kowloon, Hong Kong. China
Email: sam.feng@polyu.edu.hk

August 2018

ABSTRACT:

Flexible barriers have been widely applied in rockfall mitigation in recent years. However, the behavior of flexible barriers under the impact of boulders is still not fully understood. To investigate the interaction between a flexible barrier and a falling boulder, a large-scale physical modelling device has been constructed at a site in Hong Kong. Using this device, large-scale impact tests using boulders with different diameters were conducted. Test results are presented and analyzed in this paper. The motion of the boulder during impact is traced and analyzed. The impact forces on the flexible ring net and the supporting structures are measured and compared. From the comparison, the Impact Reduction Rates (IRR) of boulders with different diameters are calculated. Moreover, a simple approach for estimating the impact loading of a boulder on a flexible barrier is proposed in this study. This approach is calibrated and verified using measured impact forces in the tests.

Keywords: Flexible barrier; Impact loading; Simple approach; Rockfall; Large-scale physical model

1. INTRODUCTION

Rockfall is one of the most common natural hazards in mountainous areas with the features of high frequency and unpredictability (Labiouse *et al.* 1996; Matsukura 2001; Wang and Cavers, 2008; Su *et al.* 2017a; Su *et al.* 2017b; Mavrouli *et al.* 2017). Without suitable mitigation measures, falling boulders can cause disastrous damage to human habitats (Volkwein *et al.* 2011; Spadari *et al.* 2012). Protective systems such as flexible barriers and concrete dams are installed in high-risk areas to prevent damage from rockfalls. Compared with traditional concrete dams, flexible barriers have some obvious advantages: low-cost, easy-installation, and good replaceability of components (Ashwood and Hungr, 2016). In the Swiss and Europe guidelines (Buzzi *et al.* 2015; Volkwein *et al.* 2005), the kinetic energy of the falling boulder is used to determine the retention capacity of the flexible barrier. Usually, the kinetic energy of a boulder is obtained from the mass and the falling speed of the boulder at the location where the mitigation system is to be installed (Chau *et al.* 2002; Volkwein *et al.* 2009). However, kinetic energy is not a reliable criterion in the design of a flexible barrier in rockfall mitigation, because, for example, the bullet effect of high-speed boulders is ignored in kinetic energy criterion (Spadari *et al.* 2012; Hambleton *et al.* 2013; Buzz *et al.* 2015; Volkwein *et al.* 2005). Thus, impact loading could be an alternative standard in the design of flexible barriers.

Large-scale physical modeling tests are preferred by many researchers in the study of a flexible barrier interacting with a boulder (Hearn *et al.* 1995; Peila *et al.* 1998 Volkwein *et al.* 2009). Hearn *et al.* (1995) conducted several prototype tests to evaluate the performances of different types of flexible barriers subjected to impacts from boulders falling from a natural slope. Peila *et al.* (1998) carried out full-scale tests on rockfall restraining nets in a specially designed test site to investigate the performance of testing barriers with the assistance of cameras. Volkwein *et al.* (2009) studied the performances of flexible barriers subjected to extreme loads by conducting field tests. Nevertheless, an optimized monitoring system of large-scale tests is required to collect comprehensive data (Gottardi and Govoni 2010).

Estimation of the maximum impact loading from the falling boulder is important for the design of protection systems (Yu *et al.* 2016). Several theoretical models have been proposed to calculate the impact force on rigid barriers (Kawahara and Muro, 2006; Zhang *et al.* 2018). However, those models are not suitable for flexible barriers, as the behavior of flexible barriers subjects to impact consists of both moving (sliding and rotating) and stretching of the rings (Nicot *et al.* 2001), which is too complicated to be predicted by theoretical models. Thus, empirical approaches were proposed based on kinetic energy dissipation (Wartmann and Salzmann 2002; Wendeler *et al*. 2006) or work-energy principle (Peila *et al.* 1998). Basic parameters of the impact mass and empirical coefficients are integrated into those empirical approaches.

This paper aims to study the dynamic interaction between a spherical boulder and a flexible barrier. Data from dynamic transducers and photographs by high-speed cameras in the tests are obtained and analyzed. A simple approach based on the work-energy theorem is proposed considering characteristics of the boulder and the flexible barrier. This approach is calibrated and verified by the results of the large-scale tests.

2. EXPERIMENTAL SETUP AND TEST PROCEDURES

2.1 Experimental instrumentation description

A large-scale test device was constructed in the Road Research Lab of The Hong Kong Polytechnic University with a length of 9.5 m, a width of 2 m, and a height of 8.3 m. The view of the experimental setup is illustrated in Fig. 1. This facility contains 4 main components: (i) a tank with the capacity of 5 m^3, (ii) a quick flip-up door, (iii) a flexible barrier with supporting structures, and (iv) a flume connecting the tank and the flexible barrier. This flume has a channel width of 1.5 m, a length of 7 m and a designed inclination of 35º. Side walls of the flume are made up of tempered glass to provide a clear observation of the falling boulder and its interaction with the flexible barrier. The prototype flexible barrier has a width of 2.48 m and consists of steel rings with a diameter of 300 mm (No. ROCCO 7/3/300, Geobrugg), which are commonly used in rockfall mitigation in Europe and Hong Kong.

2.2 Instrumentation

To monitor the performance of a flexible protection system under the impact of a boulder, a well-arranged high-frequency monitoring system was established. Two types of transducers were installed on the flexible protection system: mini tension link transducers on the flexible ring net and high capacity tension link transducers on the supporting cables. Ten mini transducers were installed on the flexible ring net to measure the impact loading directly on the barrier. Those mini tension link transducers were self-designed and calibrated with a maximum loading of 20 kN. The central area of the ring net was separated from surrounding rings and reconnected to the ring net by mini tension link transducers. The arrangement of the transducers is plotted in Fig. 2. On the other hand, high capacity tension link transducers with the type name CFBLBH and the certified capacity of 50 kN were installed on the supporting cables to measure tensile forces on the supporting structures (see Fig. 1(c)). A data-logger with the model name of NI PXIe-1082 (National Instruments) and the capability of recording 48 transducers at 1000 Hz was used to record dynamic signals of all the transducers. Two high-speed cameras capable of taking photographs at a resolution of 1024 ×768 pixels and a sampling rate of 1000 frames per second were installed to capture the boulder motion and the impact process. The arrangement of the high-speed cameras is plotted in Fig. 1(b).

2.3 Test procedures

Two tests using spherical boulders with the diameters of 400 mm (Test 1) and 600 mm (Test 2) were conducted. In each test, the spherical boulder was released from the upper tank, accelerated along the flume, and finally trapped by the flexible barrier. The tank is 4 m higher than the bottom cable of the flexible barrier. Basic parameters of the two testing spherical boulders are listed in Table 1. The signals of all the transducers were recorded before the test to obtain initial values. Starting time of the impact has been readjusted to 0 s in all plotted data and selected video frames, and the negative value of time represents the moment before the impact. High-speed cameras were triggered at the instant before the impact to capture the impact process in detail.

3. EXPERIMENT RESULTS AND ANALYSIS

3.1 Experiment results of Test 1 (boulder diameter of 400 mm)

Forces of all the mini tension link transducers in Test 1 are plotted in Fig. 3(a). Two obvious impacts are observed, and the largest impact loading appears in the first impact. Besides, compression forces occurred in some transducers (e.g. Transducers 6, 8 and 9) during and after impact. Based on the photographs taken by the high-speed cameras, the compression forces result from the swing and torsion of the ring net during and after the impact. The tensile force peaks in all transducers are plotted in Fig. 3(b). The loading peaks range from 1.93 kN (Transducer 4) to 12.4 kN (Transducer 9). The signal of Transducer 10 combined with typical photographs at different times is plotted in Fig. 4 to explore the relationship between the impact process and force change on the barrier in Test 1. To clarify the interaction between the flexible barrier and the impacting boulder, we use white dotted lines to profile the outline of the flexible barrier at different moments and use red circles to represent the impacting boulder at different moments. It can be found from the figure that the largest deformation of the barrier, as well as the largest tensile force on the transducer appears at t=0.124 s. After that, the boulder is bounced back due to the recovery of the elastic deformation of the ring net, which causes the second impact at t=1.398 s. The peak value of the second impact is only 3/5 of the first impact. The double-impact phenomenon was also observed in full-scale tests presented by Gottardi and Govoni (2009), which indicates that the large deformation of the flexible barrier can recover well after impact, and the kinetic energy of the impact boulder can partly transform into the elastic energy of the barrier. From the continuous photographs by the high-speed camera, the motion trail and the velocity of the boulder and its interaction with the flexible barrier during the impact are plotted in Fig. 5. It can be observed that the boulder moves down and decelerates during the impact and reaches the maximum displacement of 0.877 m. After that, it is bounced back and accelerated again by the deformation recovery of the flexible barrier.

3.2 Experiment results of Test 2 (boulder diameter of 600 mm)

Forces on all the mini tension link transducers installed on the ring net in Test 2 are plotted in Fig. 6(a). Compression forces are also recorded by some transducers in this test (e.g. Transducers 5, 6, 9 and 10). Interestingly, triple impact peaks are obviously observed in some transducers (Transducers 1, 2, 5, 10). Peak loadings of all the mini transducers are plotted in Fig. 6(b). The signal of Transducer 10 combined with typical frames at different times is plotted in Fig. 7 to explore the relationship between the impact process and force change on the barrier in Test 2. It can be observed that the boulder was bounced up twice by the recovery of the elastic deformation of the flexible ring net to further reduce the impact force on the flexible barrier. Three impacts occurred at the times of 0.074 s, 1.490 s and 2.554 s, respectively. It can be concluded that the flexible barrier can decompose a large impact into multiple smaller impacts by its large elastic deformation capacity, and more impact peaks can be observed when the barrier is impacted by a mass with higher kinetic energy.

3.3 Direct measurement of the impact force on the barrier

As mentioned above, the central area is connected to neighboring net rings by mini tension link transducers. The measured maximum tensile forces on the mini transducers are used to calculate the maximum impact force on the flexible ring net. The deformation in the measured area is assumed cone symmetric to simplify the calculation. Due to the interlaced arrangement of the rings, Transducers 2, 3, 5, 6, 9, and 10 are not perpendicular to the edge of the measured area. Thus, orthogonalization is processed on the tensile forces on those transducers before they are used in the impact force calculation:

$$F_i^{'} = \cos 45° \cdot F_i \tag{1}$$

where i=2, 3, 5, 6, 9 and 10.

Thus, the impact force can be calculated with the following equation:

$$F_{impact} = \cos\frac{\theta}{2} \cdot \left(\sum F_i^{'} + \sum F_j\right) \tag{2}$$

where F_{impact} is the total impact force, θ is the included angle in the measured area bent by the impact mass, $F_i{'}$ is the orthogonalized maximum tensile force of Transducer i (Transducers 2, 3, 5, 6, 9 and 10), and F_j is the maximum tensile force of Transducer j (Transducers 1, 4, 7 and 8). The included angle of the curved ring net is measured from the photos taken at the moment of the largest deformation (see Fig. 8(b) for Test 1 and Fig. 9(b) for Test 2). The maximum impact loadings on the flexible ring net in the two tests are listed in Table 1.

3.4 Calculation of the impact force transferred to the posts

The flexible ring net is supported by two steel posts that can rotate in the plane of impact, and each post is supported by two inclined steel strand cables. Tensile forces on the strand cables are measured by the installed tension link transducers. Therefore, the maximum impact force transferred to the supporting structures can be calculated by decomposing the maximum tensile forces on the supporting cables in the direction parallel to the impact. From the arrangement of the cables plotted in Fig. 1(a) and (b), Eq. 3 is derived:

$$F_{residual} = \frac{h_{post}}{h_{impact}}\left(\sin 66^{\circ} \cos 60^{\circ} F_{B(sum)} - \sin 28^{\circ} \cos 76^{\circ} F_{A(sum)}\right) \tag{3}$$

where $F_{residual}$ is the residual force transferred to the supporting structures, h_{post} is the distance between the rotation fulcrum of the post and the connecting point of the cables, h_{impact} is the position vector from the rotation fulcrum of the post to the equivalent concentrated impact force, and $F_{A(sum)}$, $F_{B(sum)}$ are the sums of the tensile forces on cable A and cable B located at both sides. Parameters for the calculation are obtained from Fig. 8 and Fig. 9 and listed in Table 1 together with the calculated results $F_{residual}$.

Thus, the Impact Reduction Rate (IRR) of the flexible barrier is defined as:

$$IRR = \frac{F_{impact} - F_{residual}}{F_{impact}} \cdot 100\% \tag{4}$$

IRR values of Test 1 and Test 2 are calculated and presented in Table 1. The flexible barrier reduces 32% and 27% of the total impact loading in Test 1 and Test 2, respectively. With further verification, the IRR values can be used to optimize the design of flexible protection systems by estimating impact forces on the supporting structures more accurately.

3.5 A new simple approach for maximum impact loading estimation

In this section, a simple approach is proposed based on the work-energy theorem. By ignoring the transformation from kinetic energy to thermal energy during the impact, all the kinetic energy loss of the boulder equals to work done on it, and Eq. 5. is written as follows:

$$\int_0^s F_{estimated} \cdot ds = \frac{1}{2} m v^2 \tag{5}$$

where $F_{estimated}$ is the estimated impact force, s is the displacement of the boulder during the impact, m and v are the mass and the impact velocity of the boulder.

In Eq. 5, the kinetic energy of the impact boulder is easy to be obtained in the design. Normally, the designer will estimate the maximum diameter of the potential falling boulders ($d_{boulder}$) in the risky area by geological investigation, then its mass can be estimated by:

$$m = \frac{4}{3}\pi\left(\frac{d_{boulder}}{2}\right)^3 \cdot \rho_{boulder} \tag{6}$$

The impact velocity (v) can be estimated by numerical simulation considering the geometric condition of the protection area. However, it is difficult to obtain ds during the impact because of the complex motion of the boulder (as shown in Fig. 5). Hence, two coefficients: S and D are introduced in this approach. S represents the equivalent stiffness of the flexible barrier, which is a constant parameter of a type of standard flexible barriers installed with similar initial elongations. In this paper, Test 1 is used to determine the coefficient S of the used flexible barrier. The other coefficient $D = d_{boulder}{}^{-2}$ is proposed to consider the influence of the impact area. Thus, the impact force from a falling boulder on a flexible barrier can be estimated with the following equation:

$$F_{estimated} = SD\frac{1}{2}\left[\frac{4}{3}\pi\left(\frac{d_{boulder}}{2}\right)^3 \cdot \rho_{boulder}\right]v^2 = \frac{1}{12}\pi S\rho_{boulder}d_{boulder}v^2 \tag{7}$$

From the back calculation using the data in Test 1, S=2.76.

Data for Test 2 is used to verify this approach. By applying Eq. 7, the estimated impact force is 67.7 kN, which fits well with the measured maximum impact force on the flexible ring net (72.4 kN). Thus, this simple approach can be preliminarily proved feasible. By applying this simple approach, the designed impact loading of rockfalls can be easily estimated using basic parameters of possible falling boulders and the selected type of barriers. The stiffness parameter S of a standard flexible barrier can be determined by conducting a calibration test on each type of standardized flexible barriers.

4. CONCLUSIONS

In this study, large-scale physical modeling tests were conducted using spherical granite boulders with different diameters to impact a flexible barrier. Spherical granite boulders with the diameter of 400 mm (Test 1) and the diameter of 600 mm (Test 2) were used in the impact tests to study the performance of a flexible barrier subjected to falling boulders with different diameters. The interactions between the boulders and the flexible barrier have been clearly presented and analyzed in this study. From the experiment results and their analysis, the following findings and conclusions are summarized and presented:

(a) Multiple impacts were observed in Test 1 and Test 2. This phenomenon indicates that the large deformation of the flexible barrier can recover well after the first impact, and the kinetic energy of the falling boulder can be dissipated during the multiple interactions.

(b) The impact loadings on the flexible barrier and the loadings transferred to the supporting structures in the two tests were calculated and compared. It is found that the flexible barrier reduces around 30% of the total impact loadings in both Test 1 and Test 2. The design loading for the supporting structures can be accurately estimated with the help of IRR value instead of using the impact forces on the flexible ring net.

(c) A simple approach for impact loading estimation is proposed in this study. Coefficient S is proposed to represent the equivalent stiffness of flexible barriers. The data of Test 1 are used to calibrate the stiffness coefficient *S*, and the data of Test 2 are used to verify this simple approach. The calculated results using the simple approach is consistent well with the measured values.

In the future, numerical simulations using different impact velocities, testing materials, and diameters of boulders will be conducted to further verify and optimize the IRR values and the proposed simple approach.

Acknowledgement

The authors acknowledge the financial supports from Research Institute for Sustainable Urban Development of The Hong Kong Polytechnic University (PolyU). The work in this paper is also supported by a National State Key Project “973” grant (Grant No.: 2014CB047000) (sub-project No. 2014CB047001) from Ministry of Science and Technology of the People’s Republic of China, a CRF project (Grant No.: PolyU12/CRF/13E) from Research Grants Council (RGC) of Hong Kong Special Administrative Region Government of China. The financial supports from PolyU grants (1-ZVCR. 1-ZVEH. 4-BCAU, 4-BCAW, 4-BCB1, 5-ZDAF) are acknowledged. This paper is also supported by Research Centre for Urban Hazards Mitigation of Faculty of Construction and Environment of PolyU.

References

Buzzi, O., Leonarduzzi, E., Krummenacher, B., Volkwein, A., & Giacomini, A. (2015). Performance of high strength rock fall meshes: effect of block size and mesh geometry. Rock Mechanics and Rock Engineering, 48(3), 1221-1231.

Chau, K.T., Wong, R.H.C. and Wu, J.J., (2002) Coefficient of restitution and rotational motions of rockfall impacts. International Journal of Rock Mechanics and Mining Sciences, 39(1), 69-77.

Hambleton, J.P., Buzzi, O., Giacomini, A., Spadari, M. and Sloan, S.W., (2013) Perforation of flexible rockfall barriers by normal block impact. Rock mechanics and rock engineering, 46(3), 515-526.

Hearn, G., Barrett, R.K. and Henson, H.H., (1995) Testing and modeling of two rockfall barriers. Transportation research record, 1504, 1-11.

Gottardi, G., & Govoni, L. (2010). Full-scale modelling of falling rock protection barriers. Rock mechanics and rock engineering, 43(3), 261-274.

Kawahara, S. and Muro, T., (2006) Effects of dry density and thickness of sandy soil on impact response due to rockfall. Journal of Terramechanics, 43(3), 329-340.

Koo, R.C., Kwan, J.S., Lam, C., Ng, C.W., Yiu, J., Choi, C.E., Ng, A.K., Ho, K.K. and Pun, W.K., (2017) Dynamic response of flexible rockfall barriers under different loading geometries. Landslides, 14(3), 905-916.

Labiouse, V., Descoeudres, F. and Montani, S., (1996) Experimental study of rock sheds impacted by rock blocks. Structural Engineering International, 6(3), 171-176.

Matsukura, Y., (2001) Rockfall at Toyohama Tunnel, Japan, in 1996: effect of notch growth on instability of a coastal cliff. Bulletin of Engineering Geology and the Environment, 60(4), 285-289.

Mavrouli, O., Giannopoulos, P.G., Carbonell, J.M. and Syrmakezis, C., (2017) Damage analysis of masonry structures subjected to rockfalls. Landslides, 14(3), 891-904.

Nicot, F., Cambou, B. and Mazzoleni, G., (2001) From a constitutive modelling of metallic rings to the design of rockfall restraining nets. International Journal for Numerical and Analytical Methods in Geomechanics, 25(1), 49-70.

Peila, D., Pelizza, S. and Sassudelli, F., (1998) Evaluation of behavior of rockfall restraining nets by full scale tests. Rock Mechanics and Rock Engineering, 31(1), 1-24.

Spadari, M., Giacomini, A., Buzzi, O. and Hambleton, J.P., (2012) Prediction of the bullet effect for rockfall barriers: a scaling approach. Rock mechanics and rock engineering, 45(2), 131-144.

Su, L.J., Hu, K.H., Zhang, W.F., Wang, J., Lei, Y., Zhang, C.L., Cui, P., Pasuto, A. and Zheng, Q.H., (2017a) Characteristics and triggering mechanism of Xinmo landslide on 24 June 2017 in Sichuan, China. Journal of Mountain Science,14(9), 1689-1700.

Su, L.J., Xu, X.Q., Geng, X.Y. and Liang, S.Q., (2017b) An integrated geophysical approach for investigating hydro-geological characteristics of a debris landslide in the Wenchuan earthquake area. Engineering Geology, 219, 52-63.

Volkwein, A., (2005) Numerical simulation of flexible rockfall protection systems. In Computing in Civil Engineering, 1-11.

Volkwein, A., Melis, L., Haller, B., & Pfeifer, R. (2005). Protection from landslides and high speed rockfall events: reconstruction of Chapman's Peak Drive. In IABSE Symposium Report (Vol. 90, No. 6, 47-54). International Association for Bridge and Structural Engineering.

Volkwein, A., Roth, A., Gerber, W. and Vogel, A., (2009) Flexible rockfall barriers subjected to extreme loads. Structural engineering international, 19(3), 327-332.

Volkwein, A., Schellenberg, K., Labiouse, V., Agliardi, F., Berger, F., Bourrier, F., Dorren, L.K., Gerber, W. and Jaboyedoff, M., (2011). Rockfall characterisation and structural protection-a review. Natural Hazards and Earth System Sciences, 11, 2617-2651.

Wang, B. and Cavers, D.S., (2008) A simplified approach for rockfall ground penetration and impact stress calculations. Landslides, 5(3), 305.

Wartmann, S. and Salzmann, H., (2002) Debris flow and floating tree impacts on flexible barriers. In Proceedings of the Conference on Natural Terrain—a constraint to development, Hong Kong 14, 125-131.

Wendeler, C., McArdell, B.W., Rickenmann, D., Volkwein, A., Roth, A. and Denk, M., (2006) Field testing and numerical modeling of flexible debris flow barriers. In Proceedings of the International Conference on Physical Modelling in Geotechnics, Hong Kong, China, 4-6.

Yu, B., Yi, W. and Zhao, H., (2018) Experimental study on the maximum impact force by rock fall. Landslides, 15(2), 233-242.

Zhang, S.L., Yang, X.G. and Zhou, J.W., (2018) A theoretical model for the estimation of maximum impact force from a rockfall based on contact theory. Journal of Mountain Science, 15(2), 430-443.

Table 1. Parameters and results for calculation.

Test name	*Test 1 (400 mm diameter)*	*Test 2 (600 mm diameter)*
h_{post} (m)	*2.7*	
Boulder diameter (mm)	400	600
Boulder density (kg/m^3)	2650	2650
Mass (kg)	90.5	305.4
Impact velocity (m/s)	7.03	7.67
h_{impact} (m)	0.35	0.58
Included angle θ (°)	32	102
$\sum F_i^{'} + \sum F_j$ (kN)	39.46	115.04
$F_{A(sum)}$ (kN)	*0.92*	*3.15*
$F_{B(sum)}$ (kN)	7.55	25.66
$F_{residual}$ (kN)	*25.8*	*52.9*
F_{impact} (kN)	37.9	72.4
IRR (%) (Impact Reduction Rate)	*32*	*27*

Figure list:

Figure 1. Sketches of the physical model in (a) side view, (b) layout view and (c) photograph of the physical model

Figure 2. (a) schematic diagram of the flexible barrier and (b) front view of the flexible barrier with installed mini tension link transducers (unit in mm)

Figure 3. (a) forces *v.s.* time and (b) the peak tensile forces on the tension link transducers between rings in Test 1

Figure 4. Interpretation of the typical video frames recorded by (a) the side-view camera and (b) the front-view camera combined with the tensile force on Transducer 10 in Test 1

Figure 5. (a) motion trail of the boulder and boulder-barrier interaction and (b) the relationship between velocity and displacement in the direction of the impact in Test 1

Figure 6. (a) forces *v.s.* time and (b) peak tensile forces on the tension link transducers between rings in Test 2

Figure 7. Interpretation of the typical video frames recorded by (a) the side-view camera and (b) the front-view camera combined with the tensile force on Transducer 10 in Test 2

Figure 8. (a) photograph at the moment of the largest deformation (side view), (b) parallel schematic view and (c) tensile forces on supporting cables in Test 1

Figure 9. (a) photograph at the moment of the largest deformation (side view), (b) parallel schematic view and (c) tensile forces on supporting cables in Test 2

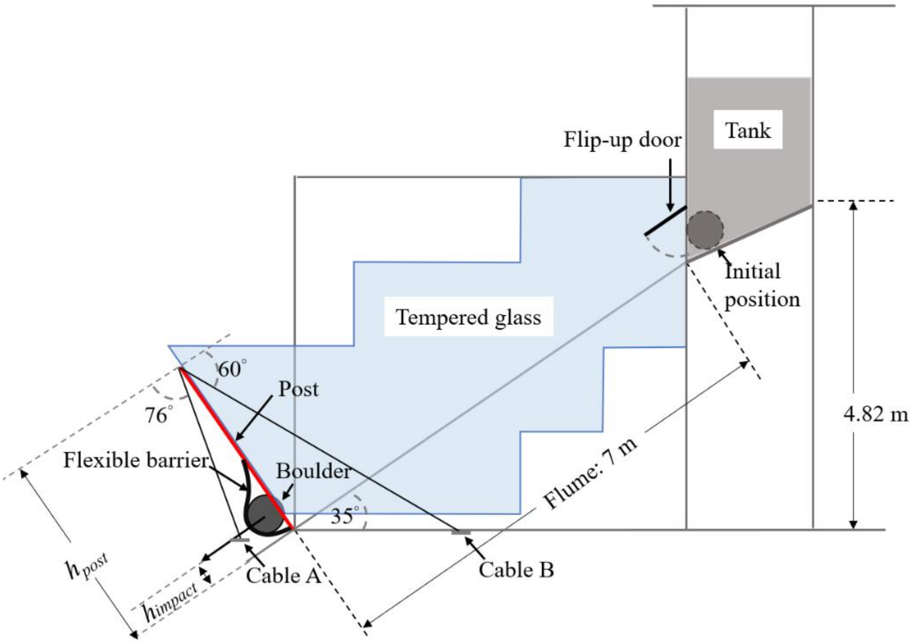
Tank
Flip-up door
Initial
position
Tempered glass
60°
76°
Post
Flexible barrier
Boulder
35°
4.82 m
Flume: 7 m
Cable A
Cable B
h_{post}
h_{impact}

(a)

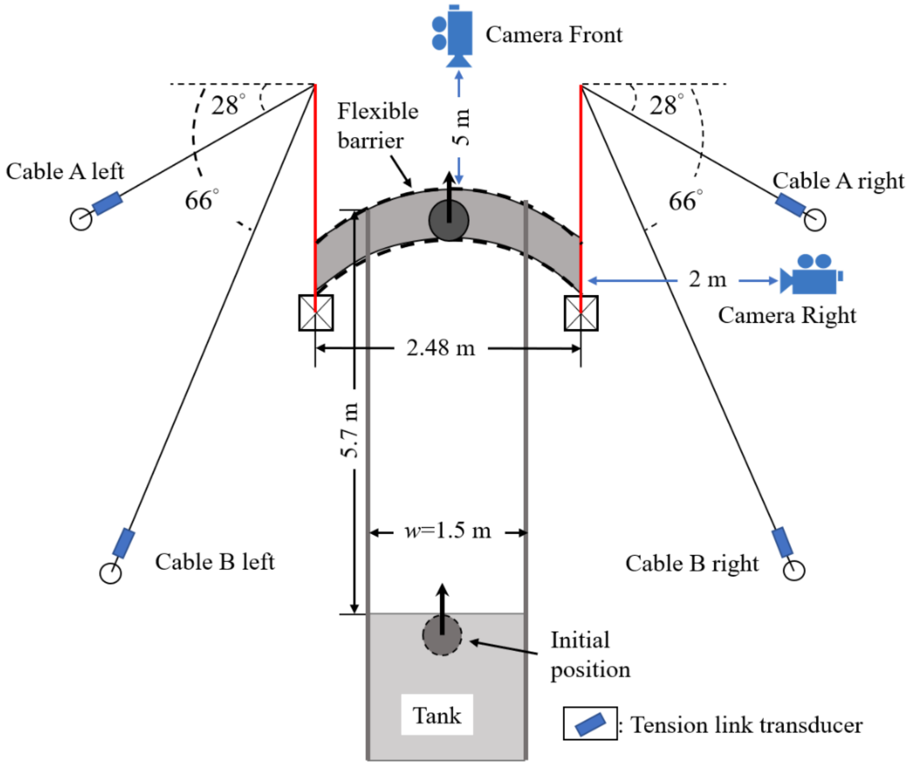
Camera Front
5 m
28°
28°
Flexible
barrier
Cable A left
Cable A right
66°
66°
2 m
Camera Right
2.48 m
5.7 m
w=1.5 m
Cable B left
Cable B right
Initial
position
Tank
: Tension link transducer

(b)

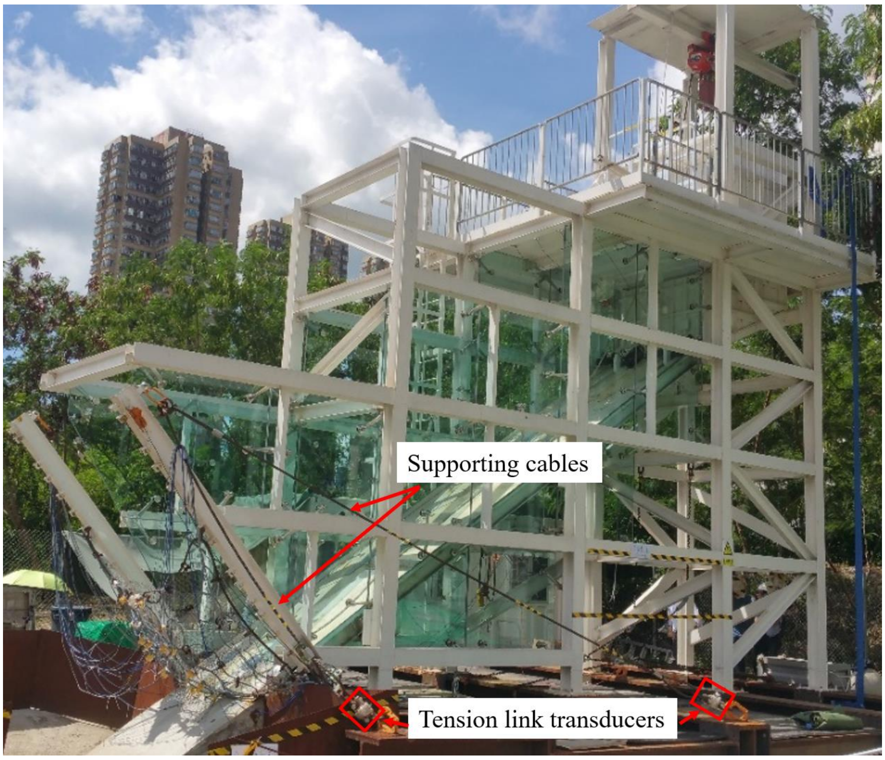

(c)

Figure 1. Sketches of the physical model in (a) side view, (b) layout view and (c) photograph of the physical model

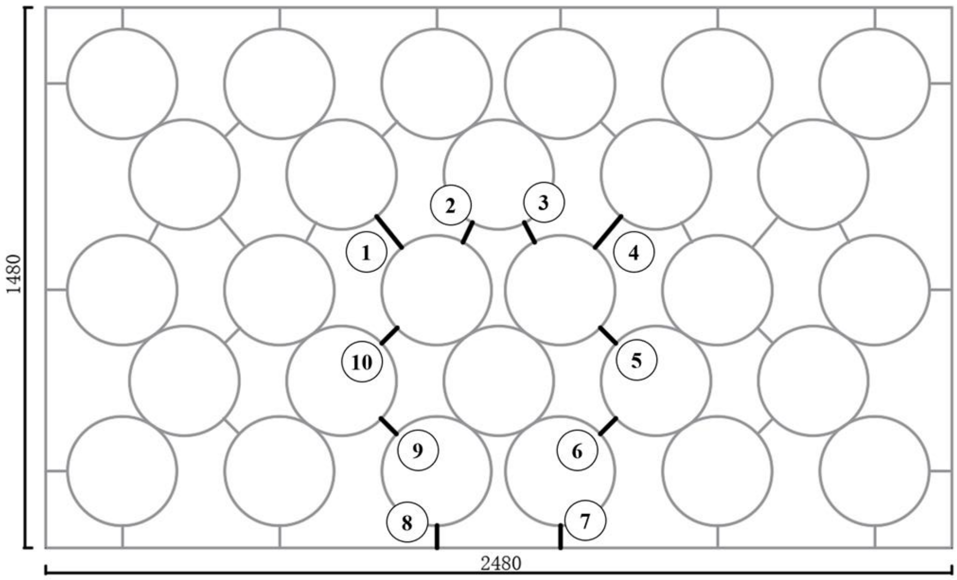

(a)

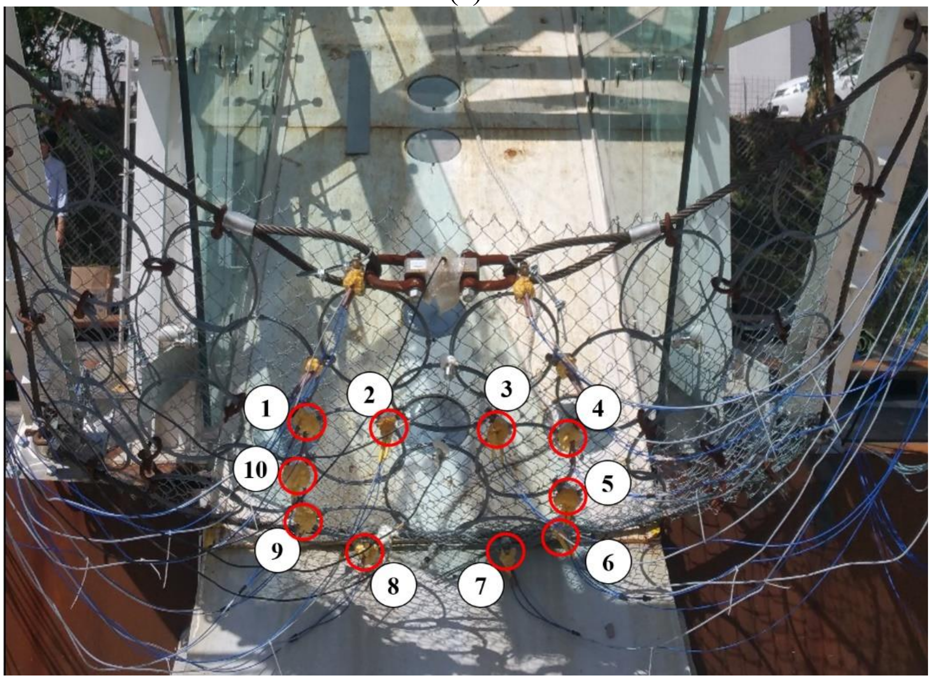

(b)

Figure 2. (a) schematic diagram of the flexible barrier and (b) front view of the flexible barrier with installed mini tension link transducers (unit in mm)

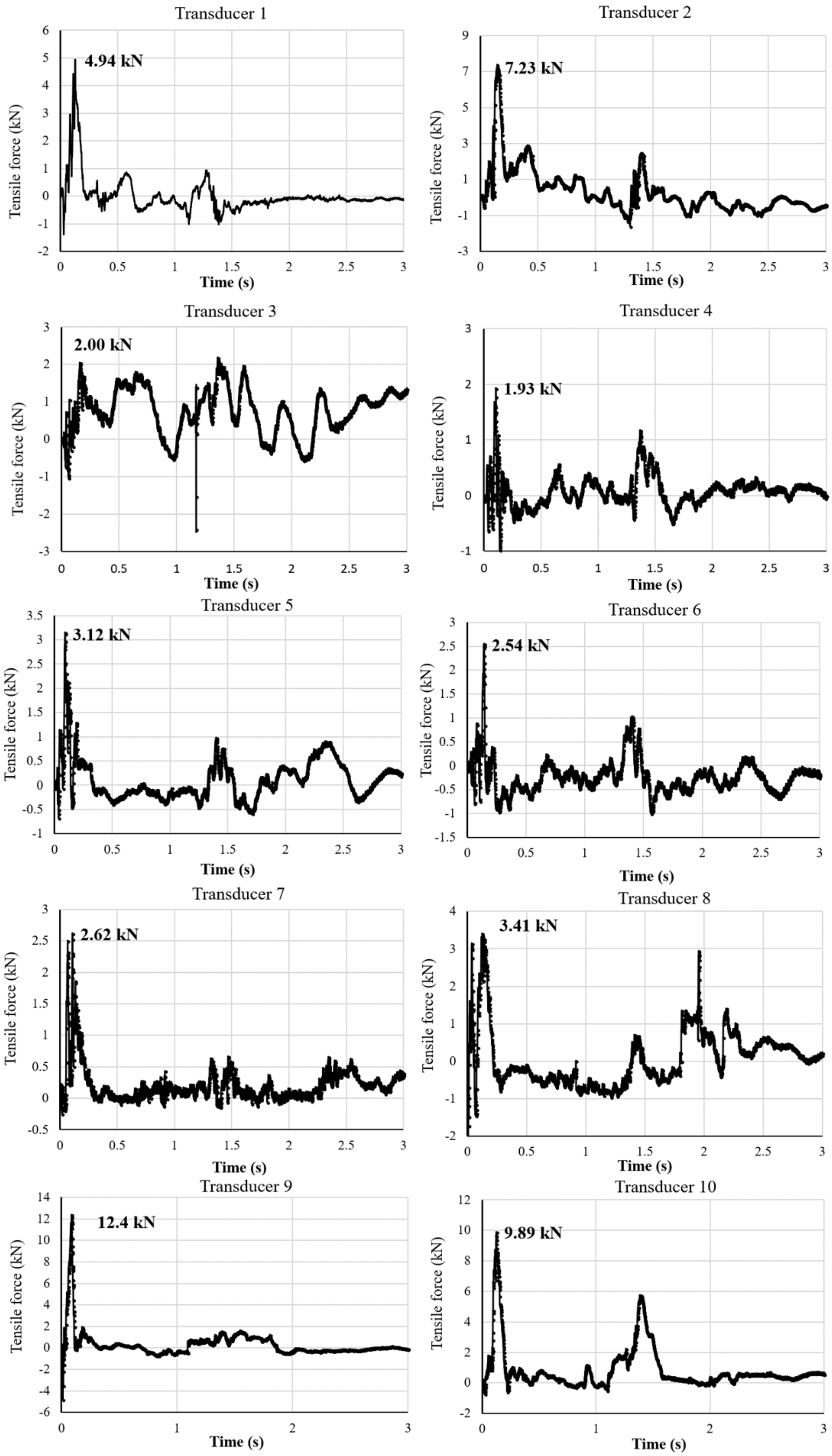

Transducer 1
4.94 kN
Transducer 2
7.23 kN
Transducer 3
2.00 kN
Transducer 4
1.93 kN
Transducer 5
3.12 kN
Transducer 6
2.54 kN
Transducer 7
2.62 kN
Transducer 8
3.41 kN
Transducer 9
12.4 kN
Transducer 10
9.89 kN
Tensile force (kN)
Time (s)

(a)

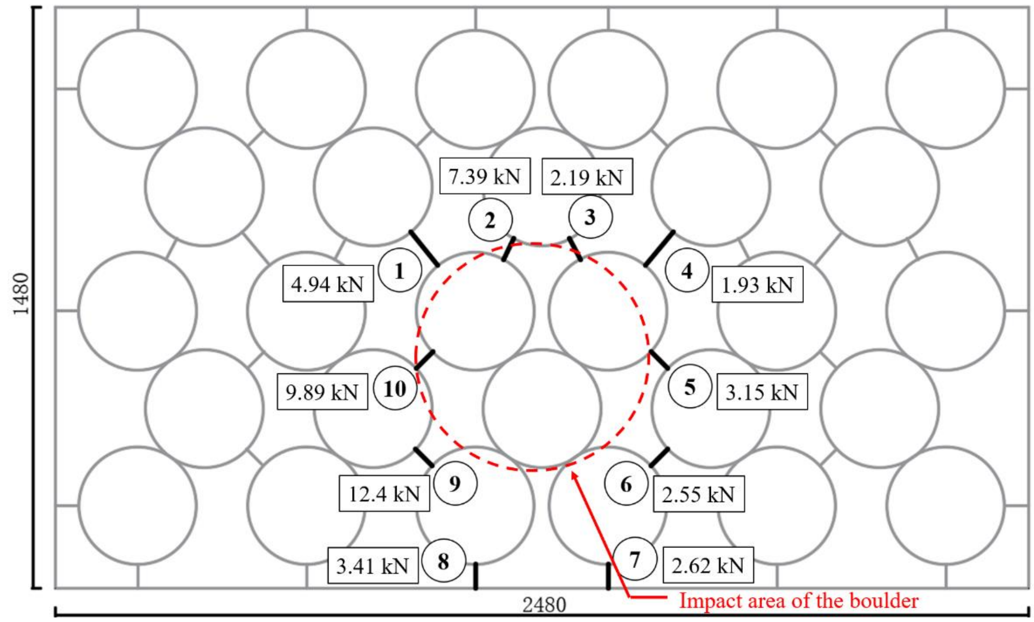

(b)

Figure 3. (a) forces *v.s.* time and (b) the peak tensile forces on the tension link transducers between rings in Test 1

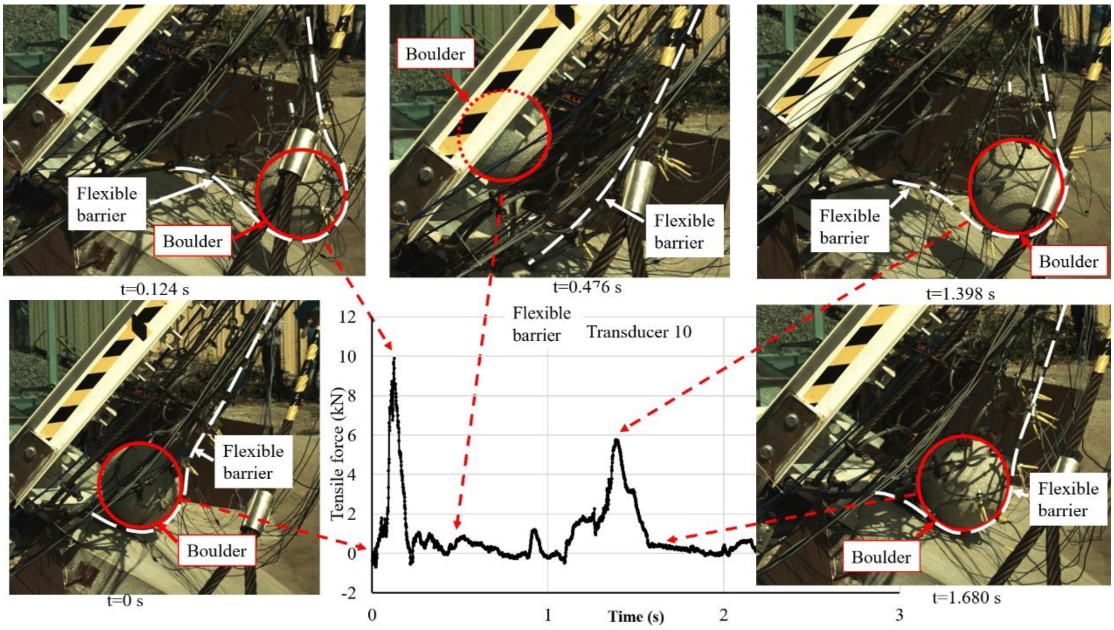

(a)

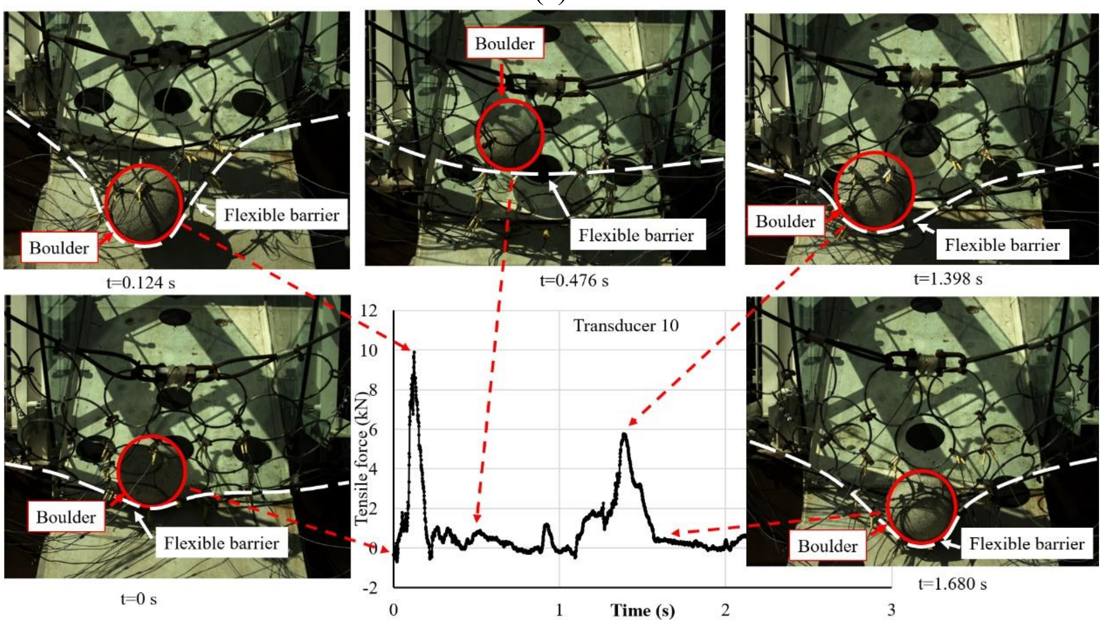

(b)

Figure 4. Interpretation of the typical video frames recorded by (a) the side-view camera and (b) the front-view camera combined with the tensile force on Transducer 10 in Test 1

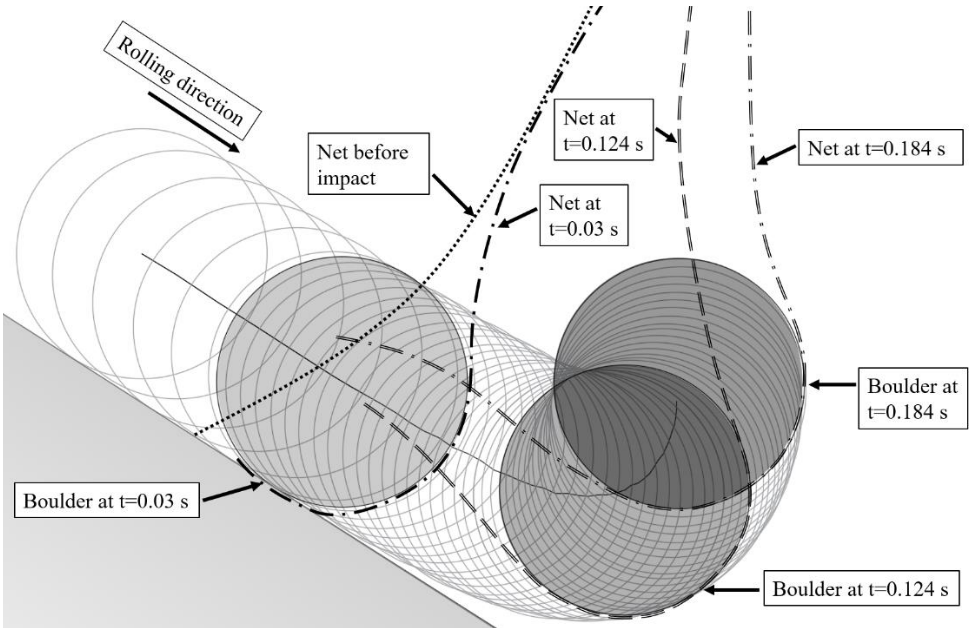

(a)

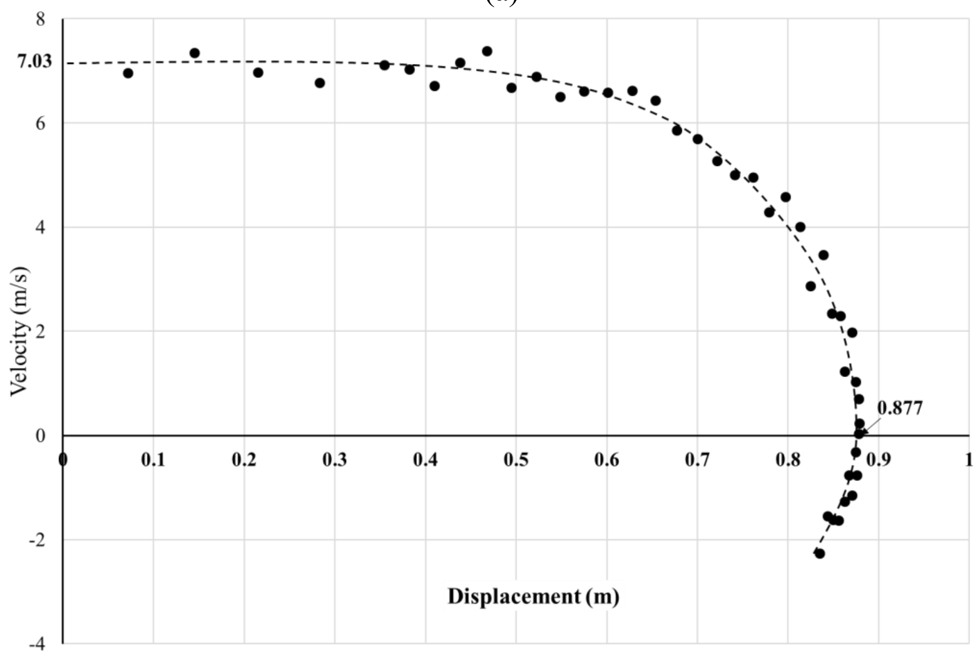

(b)

Figure 5. (a) motion trail of the boulder and boulder-barrier interaction and (b) the relationship between velocity and displacement in the direction of the impact in Test 1

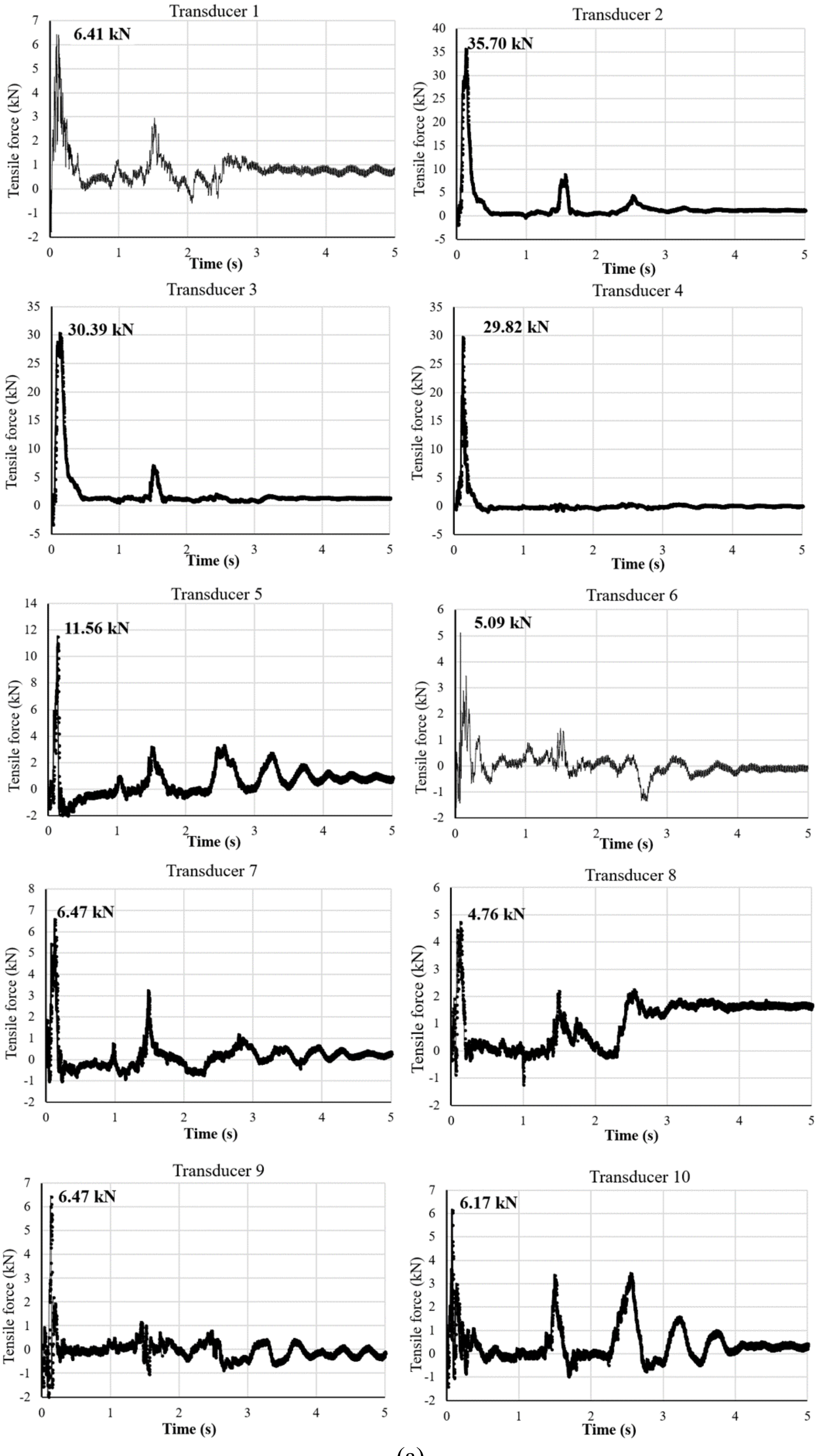
Transducer 1
6.41 kN
Transducer 2
35.70 kN
Transducer 3
30.39 kN
Transducer 4
29.82 kN
Transducer 5
11.56 kN
Transducer 6
5.09 kN
Transducer 7
6.47 kN
Transducer 8
4.76 kN
Transducer 9
6.47 kN
Transducer 10
6.17 kN
Tensile force (kN)
Time (s)

(a)

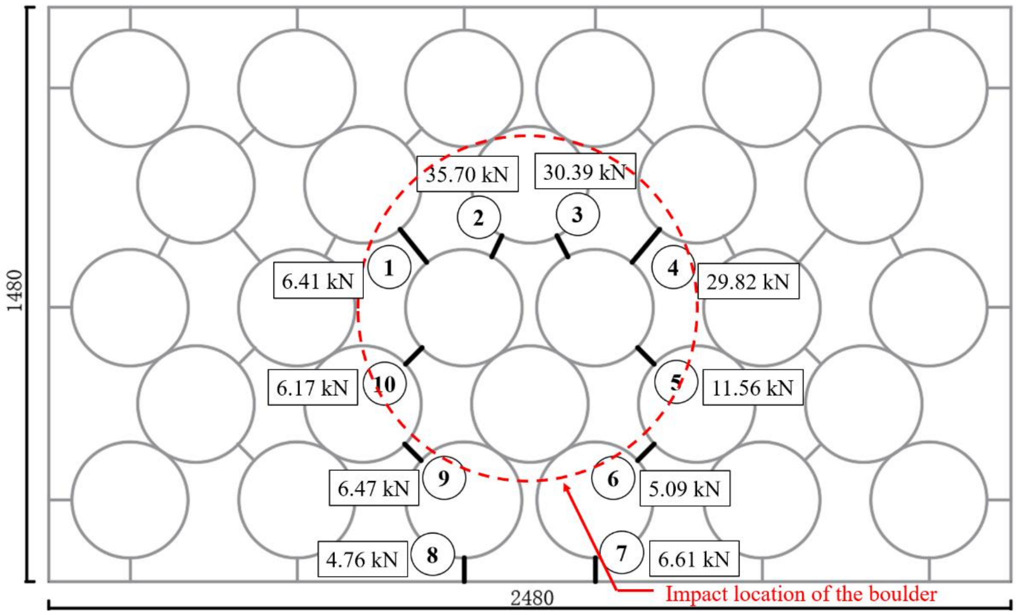

(b)

Figure 6. (a) forces *v.s.* time and (b) peak tensile forces on the tension link transducers between rings in Test 2

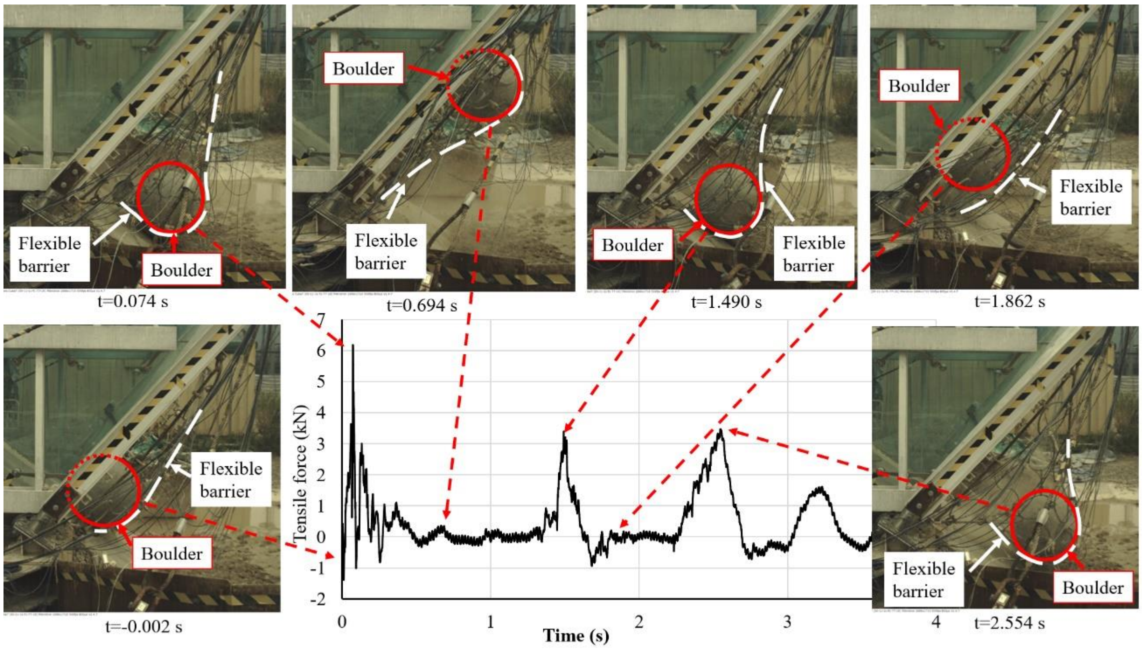

(a)

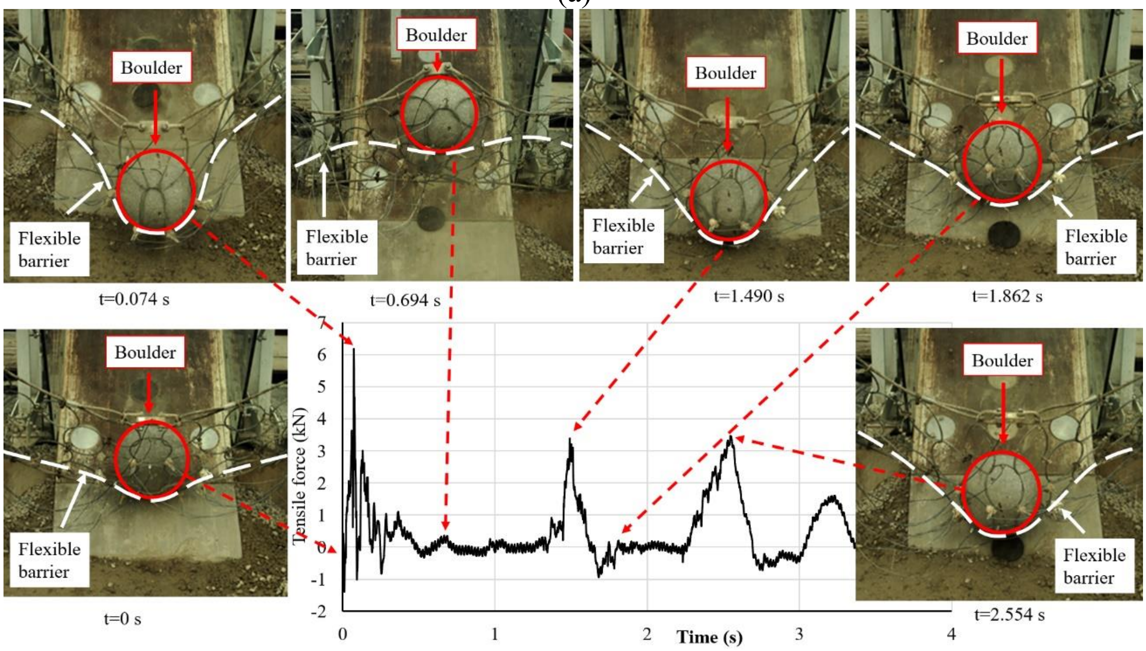

(b)

Figure 7. Interpretation of the typical video frames recorded by (a) the side-view camera and (b) the front-view camera combined with the tensile force on Transducer 10 in Test 2

436
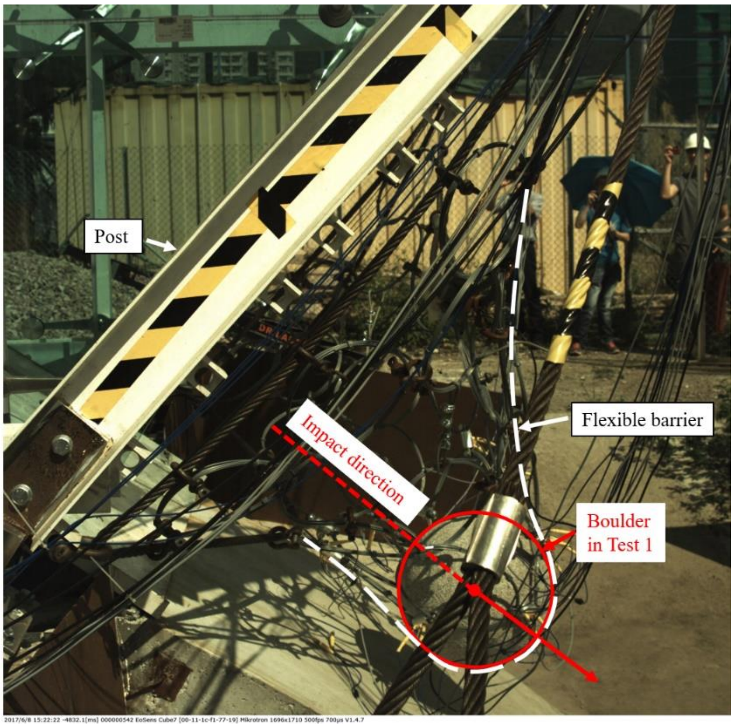

437 (a)

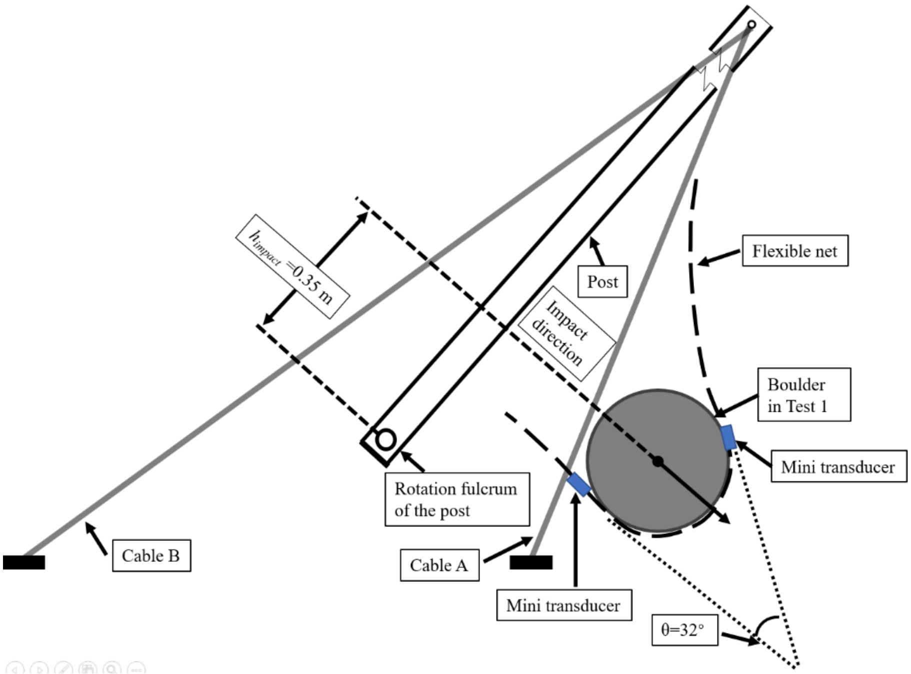

438
439 (b)

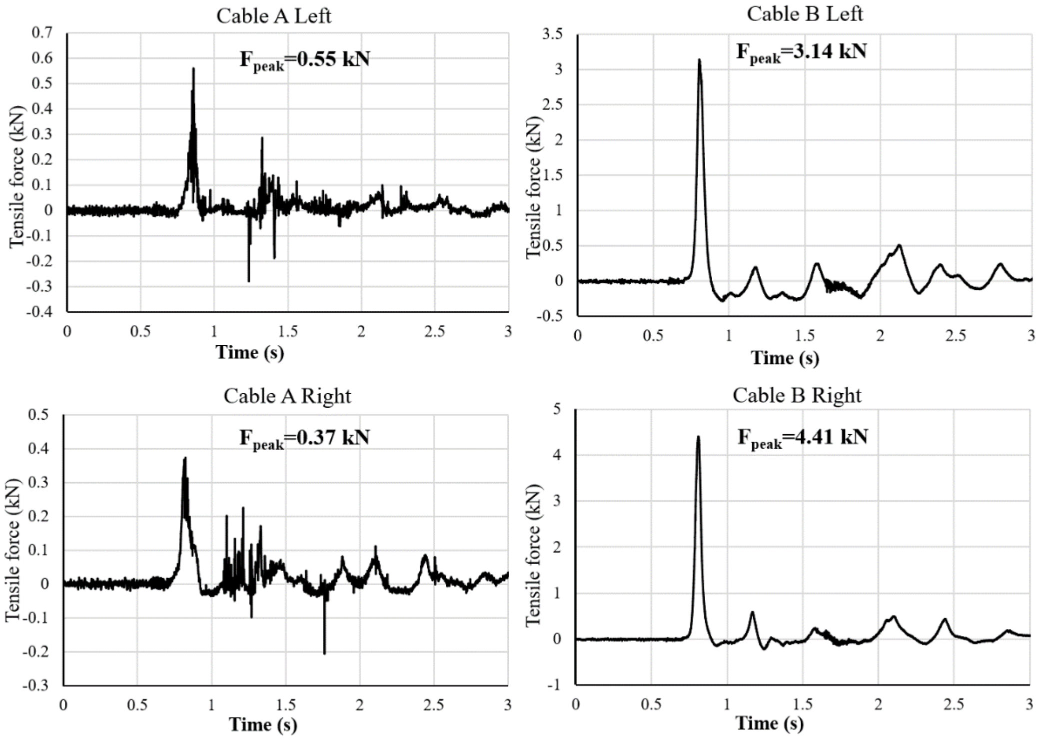

(c)

Figure 8. (a) photograph at the moment of the largest deformation (side view), (b) parallel schematic view and (c) tensile forces on supporting cables in Test 1

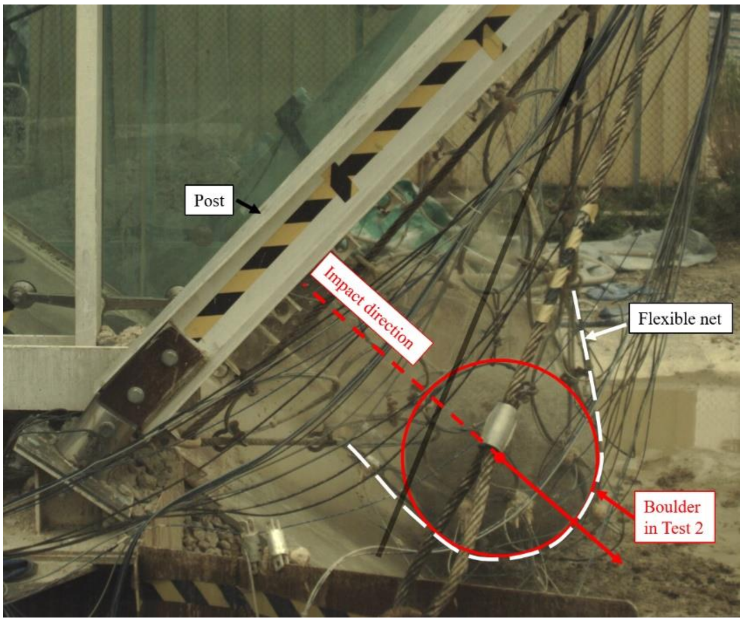
Post
Impact direction
Flexible net
Boulder
in Test 2
(a)

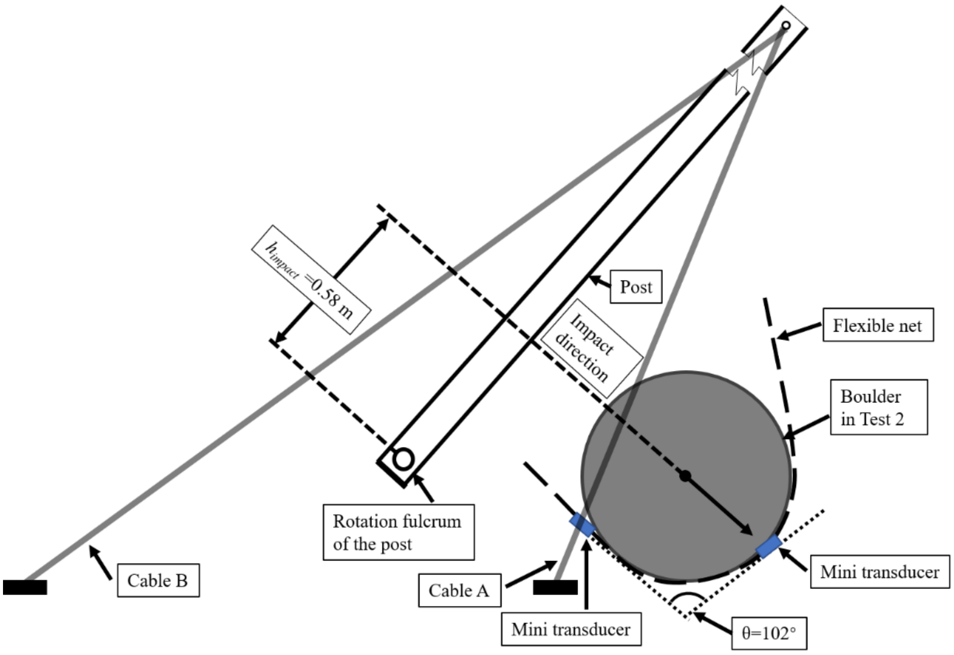
h_{impact} =0.58 m
Post
Impact
direction
Flexible net
Boulder
in Test 2
Rotation fulcrum
of the post
Cable B
Cable A
Mini transducer
Mini transducer
θ=102°
(b)

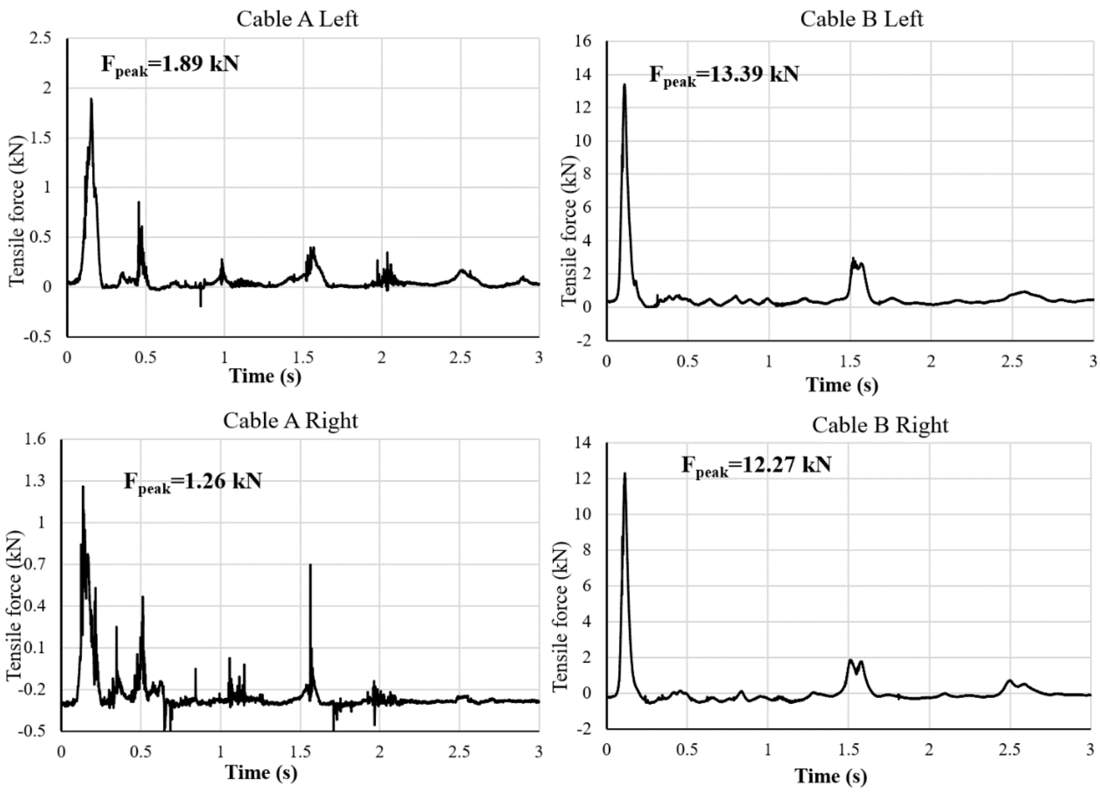

(c)

Figure 9. (a) photograph at the moment of the largest deformation (side view), (b) parallel schematic view and (c) tensile forces on supporting cables in Test 2